WJRS LETTERS

For rapid publication of innovative, leading-edge research on joining and additive manufacturing topics in the *Welding Journal Research Supplement*

Effects of Preheating on the Microstructure of Laser-DED AISI 420

The microstructural evolution of laser-DED AISI 420 was rationalized using kinetic modeling

BY Z. LYU, B. E. LONG, T. J. LIENERT, AND L. LI

■ **Keywords:** Additive manufacturing, martensitic steel, phase transformation kinetics

Introduction

AISI 420 stainless steel (420 SS) is a martensitic type known for its high strength and abrasion resistance, and it is extensively used in hard-facing applications (Refs. 1, 2). However, Type 420 SS contains untempered martensite in the as-welded condition and is generally considered to have poor weldability. Successful arc welding of 420 SS requires proper preheating, post-weld heat treatment, and strict adherence to low hydrogen practices.

Direct energy deposition (DED) is a fusion-based additive manufacturing (AM) process that melts metal powders to produce complex shapes and can be used for surfacing or hard-facing operations. However, as small-volume AM deposits undergo self-quenching, the cooling rate can be much faster than in welding. Consequently, the phase transformations in the AM deposit deviate further from equilibrium relative to traditional welding processes, resulting in heterogeneous microstructures and mechanical properties, potentially limiting the direct use of AM components without post-AM heat treatment (Ref. 3).

Our prior work with laser-DED (L-DED) hard-facing 420 SS powder without preheat combined experiments, characterization, and kinetic modeling to rationalize the presence of remnant δ-ferrite and austenite quantitatively in room temperature microstructures. This study aimed to quantify the effects of preheating above the Ms temperature on the extent of solidification segregation and microstructures for a wall build for L-DED processing of the same heat of 420 powder. The results of the current work are contrasted with our prior study, which allows for a greater understanding of L-DED opportunities with 420 SS.

Experimental Procedures

Layers of AISI/SAE 420 stainless steel powder with compositions in Table 1 were deposited using an Optomec LENS 860 direct energy deposition (DED) system with a laser power of 450 W and an incident laser spot size of approximately 1 mm with a travel speed of 7.62 mm/s. The commercial AISI 420 stainless steel powder had an unusually low Mn and slightly higher Cr than the AISI specification. Its size distribution ranged from 44 µm to 105 µm, and a series of layers, approximately 0.25 mm tall, were deposited onto a 9.5 mm-thick A2 steel substrate. The wall deposit was made with the substrate fixtured to a custom resistively-heated build plate held at 493°C (hereafter referred to as 500°C) for the entire deposit, above the reported approximate Ms, 302°C, for 420 SS (Ref. 4). The heater was turned off about 60 s after the deposits were completed, and the deposit was allowed to cool slowly to room temperature over several hours. The final wall build had a height of 20 mm, a length of 32 mm, and a width of 2 mm.

The transverse cross sections were mounted, ground, and polished according to standard metallographic procedures using a 0.25 µm diamond for the final polishing. The polished samples were electro-etched with Oxalic reagent at 6 volts for 30 s. Characterization was on a Zeiss Sigma field-emission gun scanning electron microscope (FEG-SEM) with an in-lens electron detector under 20 kV accelerating voltage, 8.5 mm working distance, and 60 µm objective aperture. In addition, energy-dispersive x-ray spectroscopy (EDS) was utilized for relative compositional analysis.

Before the electron back-scattered diffraction (EBSD) analysis, the samples were further polished with a 0.05 µm alumina suspension and 0.02 µm colloidal silica. EBSD data were collected at a step size of 0.07 µm and post-processed with HKL Channel 5 software (Ref. 5). Low-angle grain boundaries were defined as having a misorientation between 2 and

https://doi.org/10.29391/2024.103.032

Table 1 — Composition (wt-%) of Type 420 Deposit, Powder, and A2 Steel Substrate

Material	Condition	C	Cr	Mo	Si	Mn	Ni	N	P	Fe
Type 420	Nominal	0.15-0.40	12.00-14.00	N/A	1	1	N/A	N/A	0.04	Balance
A2 Steel	Nominal	0.95-1.05	4.75-5.50	0.90-1.40	0.5	1	0.3	N/A	0.03	Balance
Type 420	Powder	0.22	14.6	0.045	1.26	0.111	0.67	0.052	0.01	Balance
Type 420	Deposit	0.22	14.6	0.045	1.32	0.111	0.63	0.051	0.01	Balance

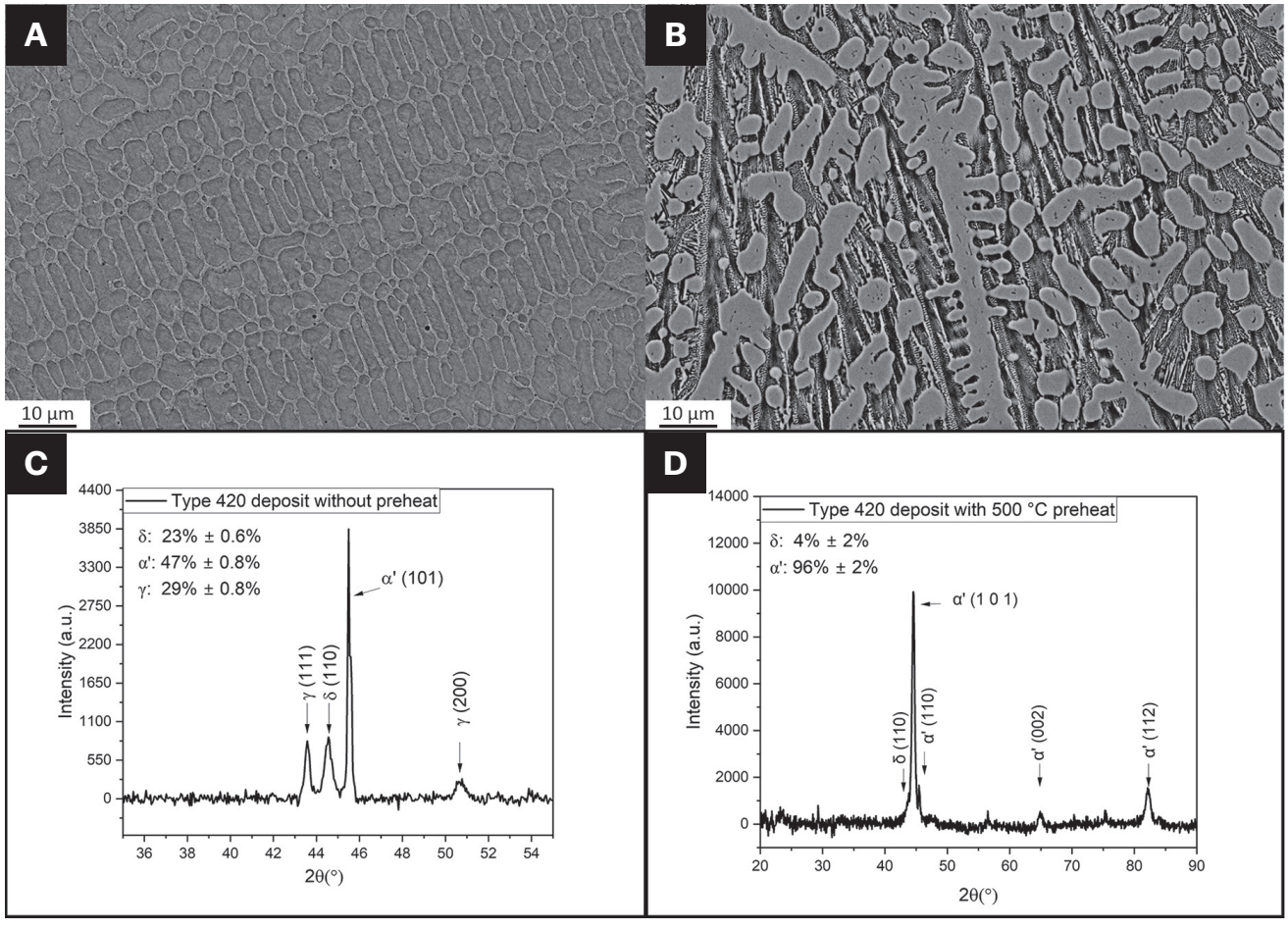

Fig. 1 — Backscattered electron microstructure of the last pass of the deposits: A — Without preheat; B — with 500°C preheat, respectively. XRD of the thin wall deposits: C — without preheat; D — with 500°C preheat, respectively. The sample without preheat was etched with Viella's reagent, while the sample with preheat was etched electrolytically with oxalic acid. Therefore, the primary dendritic phase was etched away for A, while the eutectic was etched away for B.

10 deg, while high-angle grain boundaries were defined as having a threshold misorientation greater than 10 deg.

X-ray diffraction (XRD) analysis was performed on a Bruker D8 diffractometer using a Cu (Ka) x-ray source. The scanning angle (2θ) ranged from 20 deg to 90 deg at a scanning rate of 1 deg/min. Hardness mapping was performed on a Wilson Tukon 2500 automated hardness tester with a 0.2 kgf load and 10 s of dwelling time between indentation spacings of 0.1 to 0.2 mm on an as-polished cross section.

Phase transformation kinetics calculations were performed with TCFE10 and MOBFE3 databases on Thermo-Calc software. With a domain size of 2.5 µm, both BCC and FCC phases were allowed during the peritectic reaction.

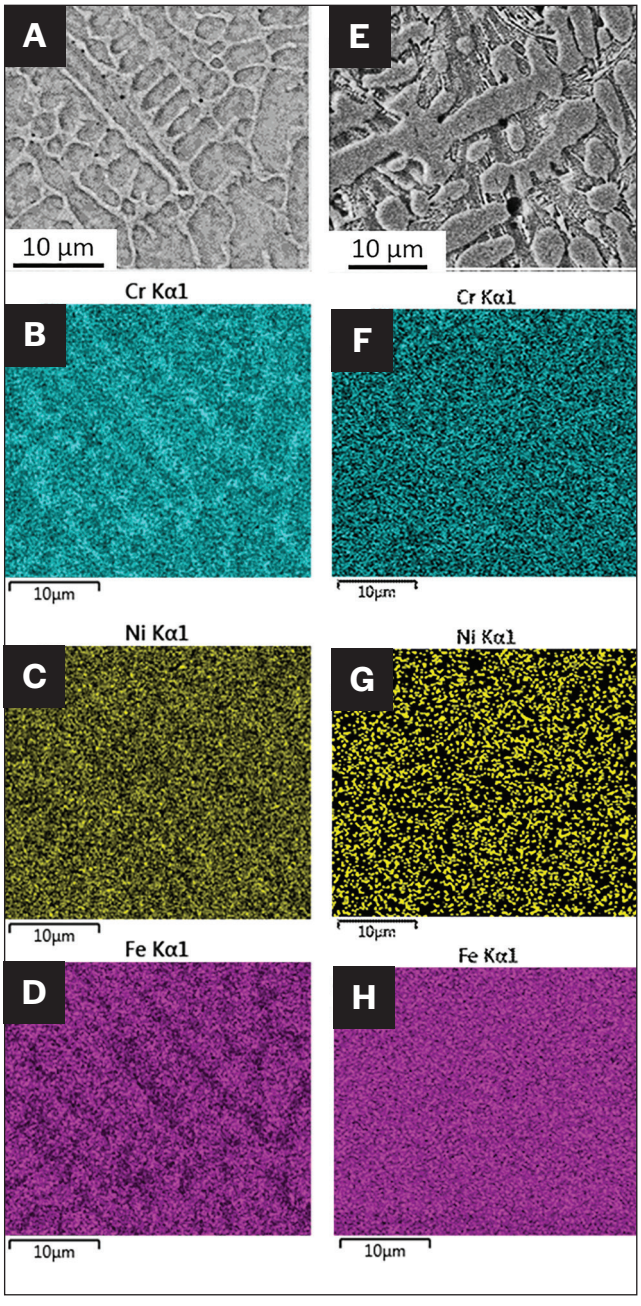

Fig. 2 — Secondary-electron image and EDS mappings of Cr, Ni, Fe, Cr, and Ni: A–D — for the deposit without preheat; E–H — for the deposit with 500°C preheat, respectively.

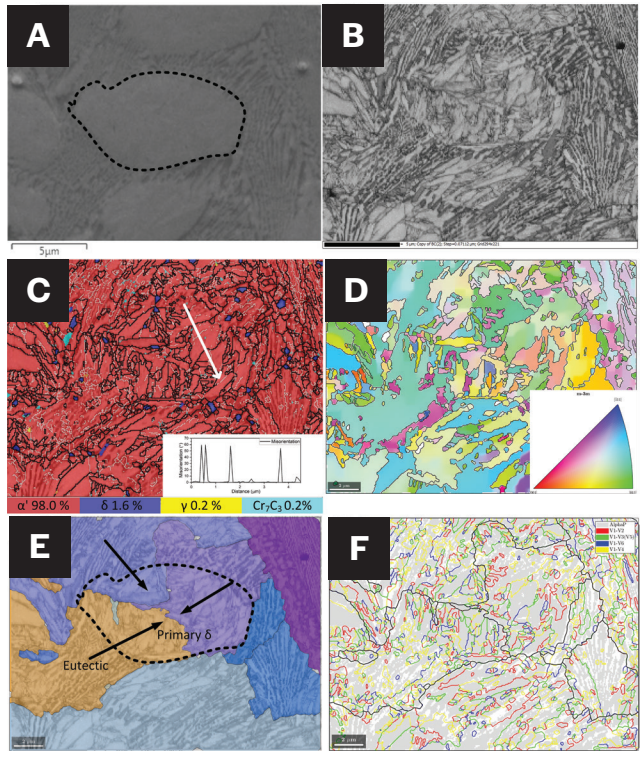

Fig. 3 — EBSD mapping of the deposit with 500°C preheat: A — BSE image of the dendrites in the as-polished condition; B — band contrast map; C — phase map after δ and α' differentiated based on GOS. The white arrow line indicates the path of the misorientation measurement, shown in the inset. D — The inverse pole figure in Z direction; E — the prior austenite grains. The black dashed lines in A and E outline a δ-ferrite dendrite. The black arrows indicate the possible growth directions of the prior austenite grains. F — The orientation variants of the martensite laths.

Results and Discussion

The microstructures of the last pass of both samples with and without preheat (Ref. 6) are shown in Fig. 1. As revealed by the backscattered-electron (BSE) image, the fusion zone of both samples primarily consisted of primary dendrites in a eutectic matrix. The SEM image in Fig. 1A showed much-finer primary dendrites and a much-smaller volume fraction of eutectics due to a faster cooling rate (without preheat) calculated at 2919 K/s, as discussed in our prior paper. The SEM image in Fig. 1B showed much coarser primary dendrites and a higher volume fraction of eutectics due to a slower cooling rate with 500°C preheat.

XRD analysis of the deposit indicated the predominant phase for the 500°C preheat sample was mostly martensite, with only 4% ferrite detected after refinement by the Rietveld technique. Conversely, the XRD analysis of the deposit without preheat consisted of three phases of similar quantities: 29% austenite, 23% ferrite, and 47% martensite (Ref. 6).

The EDS mapping of alloying elements (Fig. 2) revealed no significant elemental segregation within the deposit for the sample with 500°C preheat. However, significant Cr, Ni, and Fe segregation was observed in the sample without preheat. Preheat above the Ms decreased the degree of remnant segregation observed at ambient temperature when all other factors were kept the same.

Figure 3 presents the EBSD results for an area of 20 μm × 16 μm within the deposit with 500°C preheat. The BSE image in Fig. 3A illustrates the morphology of the primary solidified dendrites. The band contrast map, Fig. 3B, representing overall image quality, suggests that darker band contrast corresponds to regions with relatively poor diffraction quality due to lattice defects such as high dislocation densities and

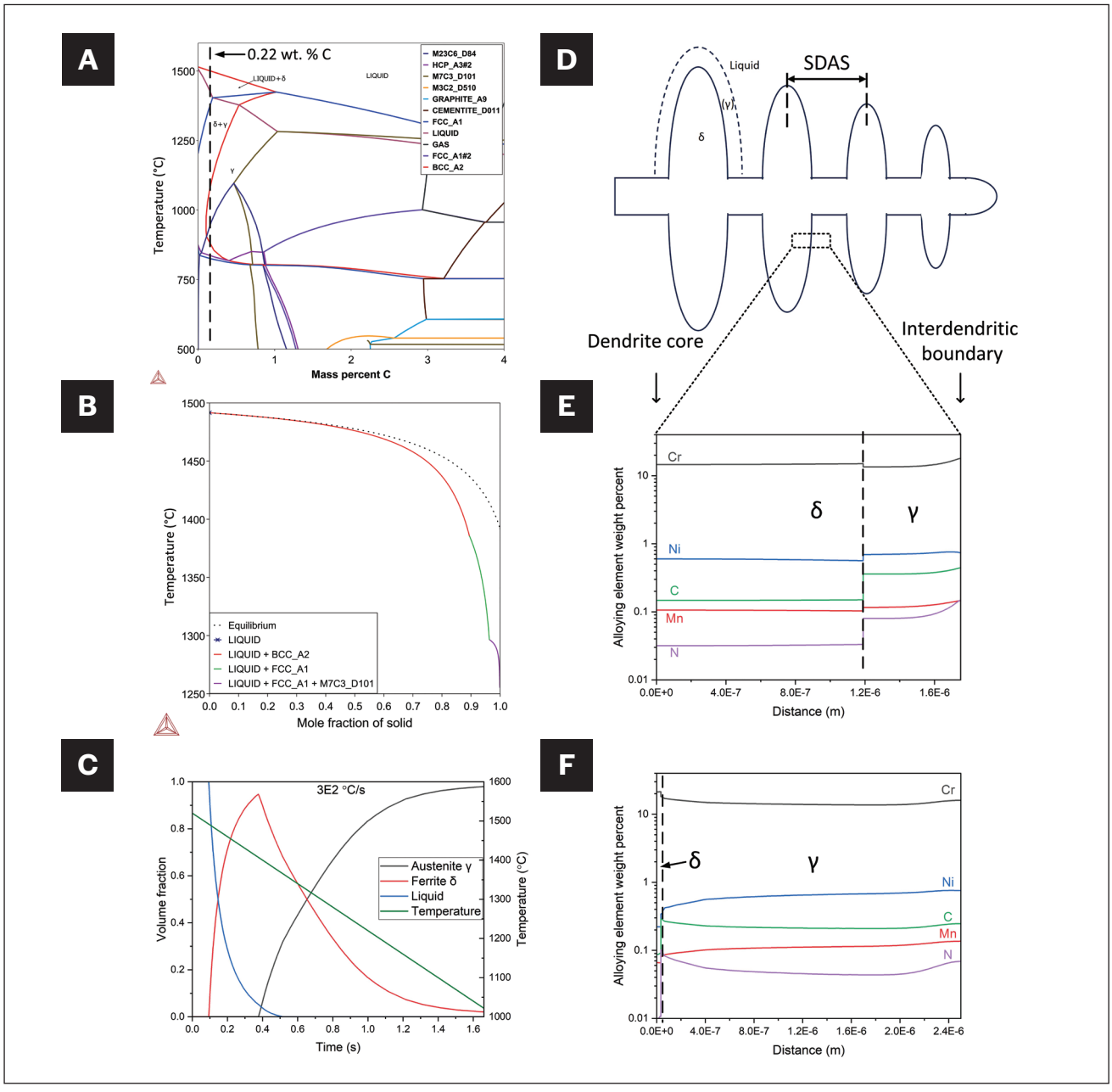

Fig. 4 — A — The equilibrium phase diagram for Type 420 stainless steel; B — Scheil solidification calculation; C — the phase quantities as a function of time during solidification for the cooling rate of 3E2°C/s; D — a schematic illustrating the DICTRA simulation domain; E — composition profiles across the simulation domain at the end of solidification; F — composition profiles across the simulation domain at 1021°C, the austenite solvus temperature.

grain boundaries (Ref. 7). The band contrast map indicates that the microstructure appears to be martensitic.

Due to the similarity in diffraction patterns from BCC-ferrite and BCT-martensite, the original EBSD phase maps indexed both phases as BCC phase (Ref. 8). Distinguishing ferrite from martensite typically requires post-processing the EBSD data, using specific characteristics as thresholds to regroup the phases. This study separated martensite from δ-ferrite using grain orientation spread (GOS) (Ref. 9) as a threshold, which measures the deviation in orientation of each point from a grain average (Ref. 10).

Grains with a GOS greater than 0.93 deg (Ref. 9) are labeled as martensite in Fig. 3D. With the updated phase map, martensite was found to be uniformly distributed. At the same time, a small portion of δ-ferrite was identified at the core of the primary dendrites and in the eutectic regions. The retained δ-ferrite at the interdendritic region suggests that the primary solidification segregation was enriched and stabilized the δ-ferrite. The δ-ferrite sizes were too small for EDS detection, consistent with findings by Salahi et al. (Ref. 11) in wire-arc-additive-manufactured (WAAM) 420 stainless steel builds.

A small fraction of retained austenite and Cr_7C_3 carbide were found at the interdendritic region as components of the eutectic at the end of solidification, as shown in Fig. 3C. Some Cr_7C_3 carbides were dispersed in the martensite matrix. Still, their sizes were ten times finer than those in the eutec-tic, suggesting solid-state precipitation during in-process tempering.

Out of all the grain boundaries observed, approximately 66% exhibited low-angle misorientation angles, ranging from 2 to 10 deg. In contrast, the remaining 34% of the grain boundaries were high angle with misorientation angles higher than 10 deg. Local misorientation along several martensite laths in Figs. 3C and F identified the Kurdjumov-Sachs Orientation Relationship Group 3 Variant pair (Ref. 12) by its distinct misorientation angle of 60 deg relative to [011] α'. Prior austenite grains have been reconstructed using the open-source EBSD analysis tool Matlab Mtex (Ref. 13). Figure 3E shows the austenite grains before the martensitic transformation, illustrating that during the δ → γ transformation, prior austenite grew from the eutectic region by inheriting the orientation of the austenite originating from solidification. Based on the orientation of the prior austenite and the IPF mapping, martensite variants were identified in Fig. 3F, validating the method to differentiate martensite by GOS.

The equilibrium phase diagram, calculated with the TCFE10 database in Thermo-Calc and shown in Fig. 4A, indicates that below the liquidus temperature of 1492°C, the 420 SS alloy solidified completely to δ-ferrite under equilibrium conditions. However, the Scheil simulation (Fig. 4B) indicates that solidification starts with primary δ forming a 90% fraction solid and forms 9% austenite γ from the liquid, with 0.9% eutectic (γ + M7C3) at the interdendritic regions. The Scheil model assumed complete mixing in the melt and no solid-state diffusion compared to equilibrium solidification.

To understand the kinetics of phase transformation and elemental segregation during continuous cooling, a diffusion-based simulation was conducted for the deposit with 500°C preheat using the DICTRA module of Thermo-Calc. This simulation accounted for diffusion in all liquid and solid phases. As depicted in Fig. 4D, the computational domain was half of the secondary dendrite arm spacing (SDAS), which was 2.5 µm from Fig. 1B. Utilizing material constants from Ref. 14, the cooling rate during solidification was estimated at 3E2°C/s. The DICTRA simulation began with 100% liquid at 1519°C, and the primary ferrite phase formed at the left end of the domain when the temperature reached the liquidus temperature of 1492°C. Subsequently, the austenite phase formed between the liquid and ferrite, consistent with the peritectic reaction (L + δ → γ). The formation of carbides at the end of solidification, as predicted by the Scheil simulation, was ignored in the diffusion model for simplicity.

The phase fractions and temperatures as functions of time are illustrated in Fig. 4C. As the temperature linearly decreased with time, δ-ferrite began to form at 0.09 s, reaching a peak volume fraction of 0.94 at around 0.37 s when peritectic austenite nucleated. Subsequently, 0.14 s later, solidification concluded with approximately 65% δ-ferrite and 35% austenite, as shown in Fig. 4E. At this finish point of solidification, evidence of minor segregation was seen within the primary δ-ferrite. In contrast, the austenite near

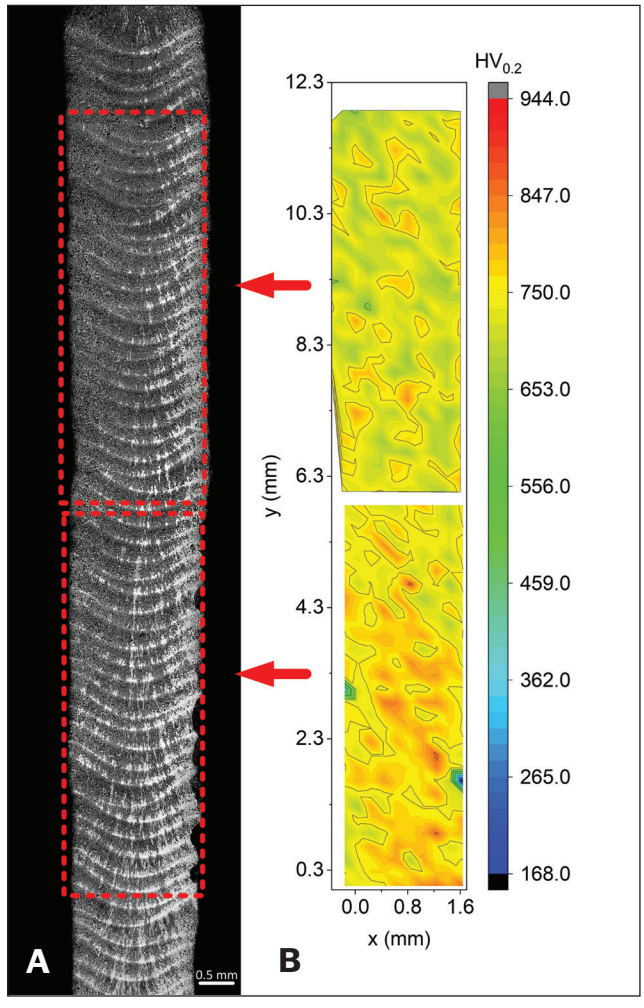

Fig. 5 — A — A transverse cross section of the thin-wall build with 500°C preheat; B — hardness mapping along the height.

the interdendritic region showed enrichment in all the alloying elements except Ni.

Further cooling transformed δ into γ as the temperature entered the δ + γ two-phase region. The simulation showed that interdiffusion of alloying elements between the dendrite cores and interdendritic regions was driven by the composition gradients resulting from solidification. At 1.66 s, as the temperature (1021°C) fell below the austenite solvus temperature, the δ → γ solid-state transformation stopped, retaining a small fraction (1.4%) of δ-ferrite until room temperature (Fig. 4F).

In contrast to the findings of our prior paper, the microstructural scale varied significantly due to a slower cooling rate (with a high preheat). Our current work revealed no retained austenite and very limited retained δ-ferrite. However, it is noteworthy that the relative microstructure remained homogeneous for the high preheat from a phase fraction viewpoint as tempered martensite (approximately 98.5%) despite the observed coarser microstructural dendrites. In contrast, the deposit without preheat had more heterogeneous phase fractions of δ-ferrite (23%), austenite (29%), and martensite (47%), despite the observed finer microstructural dendrites.

Comparing Figs. 4E and F, we found that solid-state transformation reduced the solidification segregation within the austenite. Compared with the segregation results on the deposit without preheat (Ref. 6), the homogenization progressed further for the deposit with 500°C preheat. However, it must be recognized that the eutectic products were ignored in the simulation. Consequently, the higher austenite composition at the right end of the computation domain may have been an artifact. Therefore, the martensite start temperature Ms was estimated by using the simulated composition in the center (1E-6 m) of Fig. 4F. Since the predicted Ms was 362°C (higher than reported by Abbasi-Khazaei [Ref. 4]), most austenite should have transformed into martensite upon cooling the deposit to room temperature.

As shown in Fig. 5, the deposit hardness was more uniform and without significant variations above the middle height. The average hardness of the last pass was 792 $\pm$ 48 $HV_{0.2}$, much higher than the AISI 420 (450-500 *HV*) in its as-quenched condition (Ref. 15). Compared with the hardness of the last pass deposit of AISI 420 without preheat (453 $\pm$ 120 HV0.2) (Ref. 6), the standard deviation in hardness of the high pre-heat L-DED was much smaller. Its higher hardness was attributed to the nearly complete martensite volume fraction, evidenced by the XRD results (Fig. 1D).

However, a high cooling rate is typically encountered in a typical AM process without preheating. In one of our ongoing studies on DED-built 420 stainless steel without preheating, the faster cooling rate could promote retention of 23.3% δ-ferrite and 29% austenite in the deposit. Others have reported similar inhomogeneous microstructures (Ref. 9). Furthermore, the time spent in the austenite stabilizing temperature range was reported to be too short to allow a uniform elemental redistribution (Ref. 7).

Conclusions

Martensitic stainless-steel powder of 420 SS was successfully deposited on an A2 steel substrate using laser-DED additive manufacturing. Following a 6-mm-tall deposition, the microstructure and properties achieved nearly complete homogeneity, predominantly comprising martensite, with a uniform elemental distribution confirmed by EDS analysis. The 500°C preheat environment was pivotal in promoting a median cooling rate of 3E2°C/s. Thermodynamic and kinetic calculations demonstrated that this median cooling rate effectively eliminated nearly all primary δ-ferrite and allowed the formation of austenite, which subsequently transformed into martensite. Consequently, this slower cooling rate resulted in a coarser but more homogeneous tempered martensite phase and a more-uniform hardness distribution for the laser-DED-built structure. In comparison, faster cooling (without preheat) in our prior study resulted in a softer but less-homogeneous deposit of austenite, ferrite, and martensite.

References

1. Brnic, J., Turkalj, G., Canadija, M., Lanc, D., and Krscanski, S. 2011. Martensitic stainless steel AISI 420—Mechanical properties, creep and fracture toughness. *Mechanics of Time-Dependent Materials* 15(4): 341–352. DOI: 10.1007/s11043-011-9137-x

2. Outokumpu, O. 2013. *Handbook of Stainless Steel*. Outokumpu Stainless.

3. Zhang, F., Stoudt, M. R., Hammadi, S., Campbell, C. E., Lass, E. A., and Williams, M. E. 2021. How austenitic is a martensitic steel produced by laser powder bed fusion? A cautionary tale. *Metals* 11(12): 12. DOI: 10.3390/met11121924

4. Abbasi-Khazaei, B., and Mollaahmadi, A. 2017. Rapid tempering of martensitic stainless steel AISI 420: microstructure, mechanical and corrosion properties. *Journal of Materials Engineering and Performance* 26(4): 1626–1633. DOI: 10.1007/s11665-017-2605-y

5. Schmidt, N., and Olesen, N. 1989. Computer-aided determination of crystal-lattice orientation from electron channeling patterns in the SEM. *The Canadian Mineralogist* 27(1): 15–22.

6. Lyu, Z., Lienert, T., and Li, L. 2024. Quantification of delta-ferrite and austenite retention in laser-DED deposited martensitic stainless steel. *Journal of Materials Research and Technology* 31: 2762-2773.

7. Guo, Q., et al. 2022. Phase transformation dynamics guided alloy development for additive manufacturing. *Additive Manufacturing* 59: 103068. DOI: 10.1016/j.addma.2022.103068

8. Baghdadchi, A., Hosseini, V. A., and Karlsson, L. 2021. Identification and quantification of martensite in ferritic-austenitic stainless steels and welds. *Journal of Materials Research and Technology* 15: 3610–3621. DOI: 10.1016/j.jmrt.2021.09.153

9. Gazder, A. A., Al-Harbi, F., Spanke, H. Th., Mitchell, D. R. G., and Pereloma, E. V. 2014. A correlative approach to segmenting phases and ferrite morphologies in transformation-induced plasticity steel using electron back-scattering diffraction and energy dispersive X-ray spectroscopy. *Ultramicroscopy* 147: 114–132. DOI: 10.1016/j.ultramic.2014.07.005

10. Wright, S. I., Nowell, M. M., and Field, D. P. 2011. A review of strain analysis using electron backscatter diffraction. *Microscopy and Microanalysis* 17(3): 316–329. DOI: 10.1017/S1431927611000055

11. Salahi, S., Nemani, A. V., Ghaffari, M., Lunde, J., and Nasiri, A. 2021. On microstructure, crystallographic orientation, and corrosion properties of wire arc additive manufactured 420 martensitic stainless steel: Effect of the inter-layer temperature. *Additive Manufacturing* 46: 102157. DOI: 10.1016/j.addma.2021.102157

12. Wang, Y., Kannan, R., and Li, L. 2016. Identification and characterization of intercritical heat-affected zone in as-welded Grade 91 weldment. *Metallurgical and Materials Transactions A* (47)12: 5680–5684. DOI: 10.1007/s11661-016-3736-8

13. Niessen, F., Nyyssönen, T., Gazder, A., and Hielscher, R. 2022. Parent grain reconstruction from partially or fully transformed microstructures in MTEX. *Journal of Applied Crystallography* 55(1): 180–194. DOI: 10.1107/S1600576721011560

14. Elmer, J., Allen, S., and Eagar, T. 1989. Microstructural development during solidification of stainless steel alloys. *Metallurgical and Materials A* 20: 2117–2131. DOI: 10.1007/BF02650298

15. Dodds, S., Jones, A. H., and Cater, S. 2013. Tribological enhance-ment of AISI 420 martensitic stainless steel through friction-stir processing. *Wear* 302(1): 863–877. DOI: 10.1016/j.wear.2013.01.007

ZHE LYU (*zlyu1@ualberta.ca*) is a graduate student and **LEIJUN LI** (*leijun@ualberta.ca*) is a professor at the University of Alberta, Edmonton, Alberta. **BENJAMIN E. LONG** (*blong@optomec.com*) is a solutions architect manager at Optomec Inc., Albuquerque, N.Mex. **THOMAS J. LIENERT** (*tjlienert@gmail.com*) is an adjunct professor at the University of Alberta and CEO of T. J. Lienert Consulting LLC, Los Alamos, N.Mex.